Materials Advances

ROYAL SOCIETY OF CHEMISTRY

PAPER

View Article Online
View Journal

Cite this: DOI: 10.1039/d6ma00263c

Unlocking the potential of a novel 2D VBC and a VBC/graphene heterostructure as efficient hosts for Li-ion batteries

Liaqat Ali,[a] Javed Rehman [b] and Chong-Wen Zhou *[a]

In this work, we employ first-principles calculations to predict the potential of a two-dimensional (2D) vanadium borocarbide (VBC) monolayer and a VBC/graphene heterostructure as promising anode materials for lithium-ion batteries (LIBs). This work introduces ternary 2D VBC and VBC/graphene heterostructures as a novel class of materials, integrating boron to provide mechanical robustness and carbon to ensure high electrical conductivity. This unique composition yields a synergistic combination of record-high capacity, metallic conductivity, and negligible volume expansion due to the graphene layer. The VBC monolayer and the VBC/graphene heterostructure are thermodynamically, mechanically, and dynamically stable, confirming their feasibility for experimental realization. Notably, the metallic nature of both systems is advantageous for facilitating rapid electronic transport during battery cycling. Remarkably, the VBC monolayer and the VBC/graphene heterostructure exhibit ultrahigh theoretical specific capacities of 1453.36 mAh g^{-1} and 820.60 mAh g^{-1}, respectively, which significantly surpass those of conventional graphite anodes. Furthermore, the low average open-circuit voltages of 0.45 V for the VBC monolayer and 0.68 V for the heterostructure ensure energy efficiency, while the low Li-ion diffusion barriers of 0.22 eV and 0.31 eV, respectively, indicate excellent ionic mobility and rapid charge–discharge kinetics. Lattice variation during maximum lithiation is small (2.57% for the VBC monolayer and 2.88% for the VBC/graphene heterostructure), confirming the robustness of the frameworks against volume expansion. Bader analysis shows strong charge transfer from Li to the VBC host, validating strong electrochemical interactions and a reversible lithiation process. These outstanding characteristics establish the VBC monolayer and the VBC/graphene heterostructure as highly promising candidates for next-generation high-performance LIBs.

Received 24th February 2026,
Accepted 8th May 2026

DOI: 10.1039/d6ma00263c

rsc.li/materials-advances

1. Introduction

The rapid industrialization and exponential growth of the global population have led to a drastic increase in energy consumption, resulting in the overexploitation of fossil fuels and subsequent environmental degradation.[1,2] To mitigate these challenges, the development of sustainable and renewable energy technologies has become imperative. Among various energy storage systems, rechargeable LIBs have emerged as the most successful and versatile solution due to their high energy density, long cycle life, lightweight nature, and environmental compatibility.[3–6] LIBs are widely utilized in portable electronic devices, electric vehicles, and grid-scale energy storage applications, offering high efficiency and reliable performance.[7–9] However, the growing demand for high-performance energy storage devices requires continuous improvements in battery capacity, rate performance, and longevity, which primarily depend on the characteristics of electrode materials, especially anodes.[10–12]

Graphite has been extensively used as a commercial anode material for LIBs owing to its high stability, low cost, and decent cycling performance.[13] Nonetheless, its low theoretical specific capacity (372 mAh g^{-1}) and structural instability during repeated lithiation/delithiation cycles limit its further application in next-generation batteries.[14–16] Alternative materials such as titanium dioxide (TiO_2), silicon (Si), and black phosphorus (BP) have been investigated to overcome these limitations. TiO_2 demonstrates excellent thermal stability and a long cycle life, yet it suffers from a low specific capacity ($\sim$200 mAh g^{-1}).[17] In contrast, Si and BP offer remarkably high theoretical capacities of 4200 and 2596 mAh g^{-1}, respectively, but their significant volume expansion during Li insertion and extraction leads to mechanical

[a] Combustion Chemistry Centre, School of Biological and Chemical Sciences, MaREI, Ryan Institute, University of Galway, Galway H91 TK33, Ireland. E-mail: chongwen.zhou@universityofgalway.ie
[b] State Key Laboratory of Metastable Materials Science and Technology, School of Materials Science and Engineering, Yanshan University, Qinhuangdao 066004, China

pulverization and rapid capacity fading.[18–20] Consequently, the search for new anode materials that combine high energy density, superior electronic conductivity, and structural stability has become a major focus of contemporary battery research.

One of the most promising strategies for enhancing LIB performance is the use of 2D materials as anode candidates. 2D materials possess atomically thin layers, large surface areas, short ion diffusion lengths, and tunable electronic properties, making them ideal platforms for electrochemical energy storage.[4,21–23] Since the discovery of graphene, numerous 2D materials, including silicene, germanene, phosphorene, transition metal dichalcogenides (TMDs), and MXenes, have been proposed and theoretically validated as high-performance electrode materials.[24–30] However, despite their excellent properties, many of these materials still face challenges. For instance, pristine graphene exhibits outstanding electrical conductivity, but its low Li storage capacity limits its application as an anode in LIBs.[31–33] Likewise, transition metal dichalcogenides (TMDs) such as $MoSe_2$ possess layered structures that are well suited for Li intercalation; however, their relatively wide band gaps and poor intrinsic conductivity can hinder rate performance. Despite these limitations, recent density functional theory studies have shown that $MoSe_2$ monolayers can achieve a theoretical capacity of 422 mAh g^{-1} with a low diffusion barrier of 0.299 eV.[34] MXenes, by contrast, exhibit metallic conductivity and strong surface reactivity, positioning them as highly competitive 2D anode materials.[27,35] Among these, carbon-rich vanadium carbides like VC_4 have demonstrated exceptional promise, with a theoretical capacity of 1353 mAh g^{-1} and Li^+ diffusion barriers as low as 0.18 eV.[36]

Recent studies have also explored binary and ternary transition metal borides and carbides due to their unique electronic and mechanical properties.[37,38] Incorporating boron (B) and carbon (C) atoms into transition metal lattices can simultaneously improve electrical conductivity, structural integrity, and ion diffusion kinetics. Specifically, vanadium-based compounds exhibit metallic characteristics and strong bonding interactions with lithium ions, making them potential candidates for anode materials.[36,39–41] Introducing boron into these systems further enhances charge transfer capability and mechanical strength, while carbon improves the overall conductivity and Li storage capacity.[42] Consequently, the design of a novel 2D VBC monolayer could combine the intrinsic advantages of borides, carbides, and vanadium-based materials, offering a promising pathway for high-performance anode development.

To further enhance electrochemical performance, constructing heterostructures that integrate 2D materials with graphene has gained considerable attention. Graphene-based heterostructures can effectively suppress volume expansion, accelerate charge transport, and provide additional active sites for Li adsorption due to synergistic interfacial effects.[43–45] For example, MoS_2/graphene and VS_2/graphene heterostructures have demonstrated superior Li storage capacity and cycling stability compared to their pristine counterparts.[46,47] Similarly, theoretical studies on SiC/graphene and V_3C_2/graphene composites have reported enhanced electronic conductivity, improved Li-ion mobility, and mitigation of structural degradation during cycling.[48,49] Therefore, the integration of a 2D VBC monolayer with graphene to form a VBC/graphene heterostructure is anticipated to further improve the electrochemical activity, mechanical stability, and rate capability of LIB anodes.

In this work, we present a first-principles density functional theory (DFT) investigation of a novel ternary 2D VBC monolayer and its VBC/graphene heterostructure as potential anode materials for LIBs. This study comprehensively examines their structural stability, electronic characteristics, Li adsorption behaviour, diffusion dynamics, and open-circuit voltage (OCV) profiles. Our findings establish the VBC monolayer and VBC/graphene heterostructure as theoretically viable, high-performance anode systems that address critical gaps in current LIB technology, offering a strong foundation for future experimental realization and device integration.

2. Computational methods

The investigation of 2D materials is commonly carried out within the framework of density functional theory (DFT), and in this work, all calculations were performed using the Vienna *Ab initio* Simulation Package (VASP).[50] The exchange–correlation interaction was described by the generalized gradient approximation in the form of the Perdew–Burke–Ernzerhof (PBE) functional,[51] while the screened hybrid functional HSE06[52] was additionally employed to obtain accurate electronic properties. A plane-wave basis set with a kinetic energy cutoff of 520 eV was adopted, and the Brillouin zone was sampled using a Monkhorst–Pack *k*-point mesh of $7 \times 7 \times 1$ to ensure convergence, as shown in Fig. S1. A vacuum spacing of 22 Å was introduced along the *c*-axis to eliminate interlayer interactions. The DFT-D3 correction was applied to accurately describe the weak van der Waals interactions between the substrate and Li atoms.[53,54] During the structural relaxations, the convergence criteria for total energy and forces were set to 1×10^{-5} eV and 0.01 eV $Å^{-1}$, respectively. Bader charge analysis was applied to evaluate the charge transfer from a single Li atom to a VBC monolayer and VBC/graphene heterostructure.[55,56] The dynamic stability of the optimized structures was verified by calculating the phonon dispersion spectra using the density functional perturbation theory (DFPT) approach[57] implemented in the PHONOPY code.[58] Thermodynamic stability was further confirmed through *ab initio* molecular dynamics (AIMD) simulations at 300 K and 500 K for a total simulation time of 10 000 fs in the NVT ensemble using a Nosé–Hoover thermostat.[59] The ion diffusion barriers were determined using the climbing image nudged elastic band (CI-NEB) method,[60] where several intermediate images were interpolated between initial and final states. The lattice mismatch between materials was evaluated using the following expression: % mismatch = (estimated lattice constant − actual lattice constant)/actual lattice constant × 100%.[36] The following equations were employed to calculate the adsorption

energy,[61] average open-circuit voltage,[62] and charge density difference:

$$E_{ad} = \frac{E_{Sub} - E_{Pristine} - nE_{Li}}{n} \quad (1)$$

where E_{Sub} is the total energy of the Li-adsorbed VBC monolayer and VBC/graphene heterostructure, $E_{Pristine}$ is the total energy of the pristine VBC monolayer and VBC/graphene heterostructure, E_{Li} is the total energy of the single Li atom, and n denotes the number of adsorbed Li atoms.

$$\Delta\rho = \rho_{Sub} - \rho_{Pristine} - \rho_{Li} \quad (2)$$

where ρ_{Sub} and $\rho_{Pristine}$ represent the charge densities of the Li-adsorbed and pristine VBC monolayer and VBC/graphene heterostructure, respectively, and ρ_{Li} is the charge density of an isolated Li atom.

$$V_{OCV} = \frac{E_{Pristine} - xE_{Li} - E_{Sub}}{xe} \quad (3)$$

where $E_{Pristine}$ and E_{Sub} denote the total energies of the pristine and Li-adsorbed VBC monolayer and VBC/graphene heterostructure, x is the number of adsorbed Li atoms, and e is the elementary charge.

3. Results and discussion

3.1. Structural analysis

VBC crystallizes in the hexagonal $P6_3/mmc$ space group. Fig. 1(a) shows the top and side views of the optimized structure of a 3 × 3 × 1 supercell of the two-dimensional VBC monolayer. After optimization, the calculated lattice parameters of the VBC monolayer are $a = b = 2.70659$ and $c = 22$ Å. All V–C bond lengths are 2.36 Å and B–C bond lengths are 1.61 Å. The surface energy (γ) offers an alternative metric for assessing the thermodynamic stability of the 2D material.[63] The surface energy was simulated with $\gamma = \frac{N_{2D}}{2A}\Delta E_f$, where ΔE_f represents the formation energy relative to the bulk ground state, N_{2D} is the number of atoms in the 2D structure unit cell, and A denotes the in-plane area of the 2D material. The calculated low surface energy of the VBC monolayer is 32.69 meV Å^{-2}, which shows that the VBC monolayer should be a potentially exfoliable 2D material. The novel VBC/graphene heterostructure is constructed by merging a 3 × 3 × 1 supercell of the VBC monolayer and a 3 × 3 × 1 supercell of graphene (Gr) with a height of 3.8 Å, to minimize lattice mismatch. The calculated lattice mismatch for the VBC/graphene heterostructure is ~10%, which is higher than that of typical 2D heterostructures of around <5%.[64] But this remains acceptable for van der Waals heterostructures, where weak interlayer interactions relax strict lattice-matching constraints.[65,66] In this study, the structure

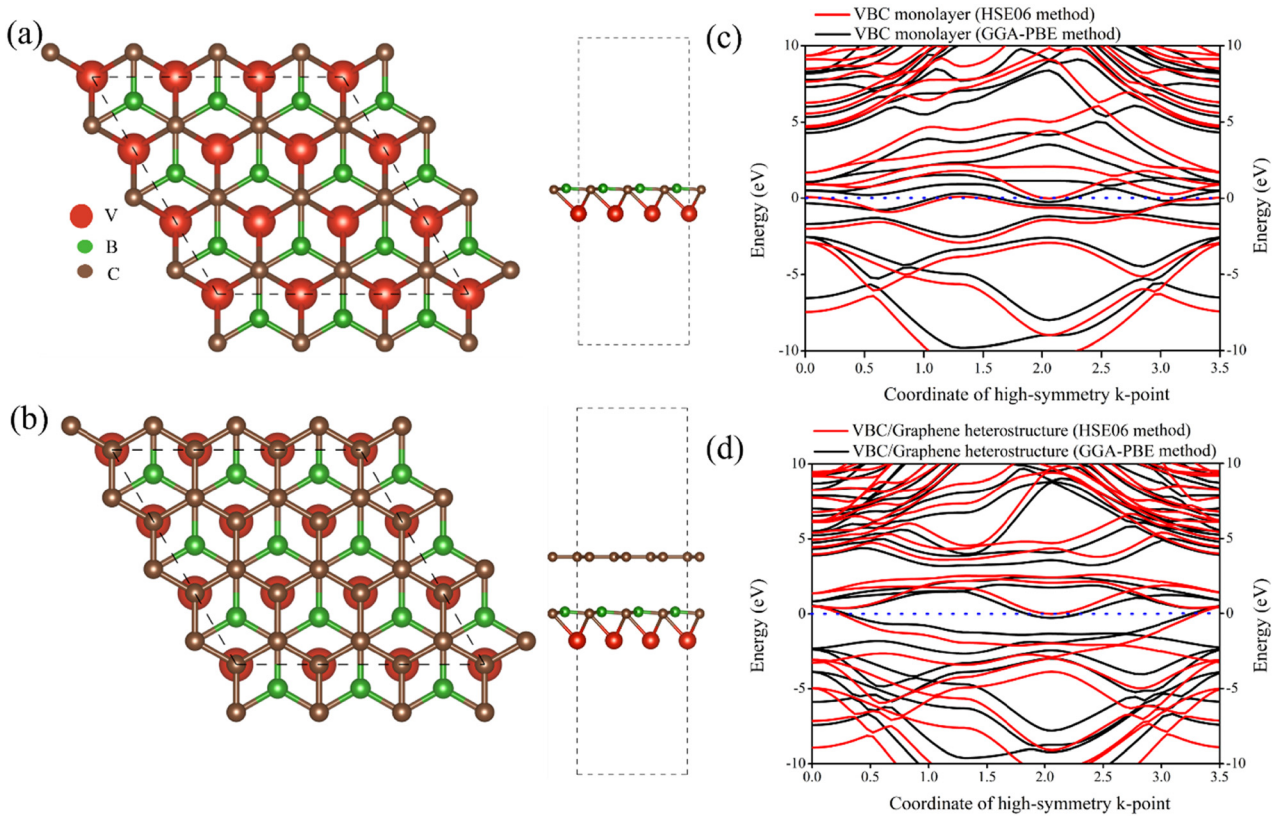

Fig. 1 Front view and side views of the (3 × 3 × 1) (a) VBC monolayer and (b) VBC/graphene heterostructure. Electronic band structures of the (c) pristine VBC monolayer and (d) VBC/graphene heterostructure calculated with the GGA-PBE and hybrid HSE06 methods.

optimization without externally applied strain yields a dynamically, thermally, and mechanically stable configuration, indicating that the lattice mismatch is intrinsically accommodated at the interface. The lattice mismatch leads to localized variations in the interfacial potential energy surface, which may slightly influence the electronic structure, charge distribution, and Li-ion migration barriers but does not significantly affect the overall stability or predicted the electrochemical performance of the heterostructure. Fig. 1(b) shows the front and side views of the VBC/graphene heterostructure with a vacuum spacing of 22 Å. After structural optimization, the calculated lattice constants are $a = b = 7.76$ Å, with a C–C bond length of 1.88 Å, respectively. Furthermore, Fig. 1(c) and (d) show the calculated electronic band structures of the VBC monolayer and VBC/graphene heterostructure using GGA-PBE and hybrid HSE06 functionals, respectively. In both cases, several energy bands cross the Fermi level, confirming the metallic nature of the system. While the overall dispersion trends are similar, the HSE06 functional provides a more accurate description of the electronic states near the Fermi energy due to the inclusion of exact exchange. The metallic character obtained from both methods suggests that the VBC monolayer and VBC/graphene heterostructure can offer high intrinsic electronic conductivity, which is beneficial for rapid charge transfer and stable cycling when employed as an electrode material in rechargeable batteries.

The bonding characteristics of the VBC monolayer and VBC/graphene heterostructure were examined using an electron localization (ELF) function, as illustrated in Fig. 2(a) and (b). The ELF color map ranges from 0 (blue, delocalized electrons) to 1 (red, highly localized electrons). An ELF value greater than 0.5 indicates covalent bonding, a value lower than 0.5 suggests ionic bonding, and a value near 0.5 corresponds to metallic bonding.[67] The ELF of the VBC monolayer shows strong localization around the B–C bonds, reflecting pronounced covalent interactions within the in-plane framework, while the regions surrounding the V atoms exhibit more moderate ELF values, consistent with partially delocalized d-electron contributions and mixed covalent–metallic bonding. In the VBC/graphene heterostructure, the ELF distribution near the interface becomes perturbed, with enhanced localization around the upper B/C atoms and the graphene carbon atoms; however, the absence of the highly localized interlayer ELF indicates that no covalent bonds form between the two layers. Instead, the electron density remains largely confined within each component, confirming that the VBC/graphene interaction is dominated by van der Waals forces, allowing both layers to retain their intrinsic electronic characteristics.

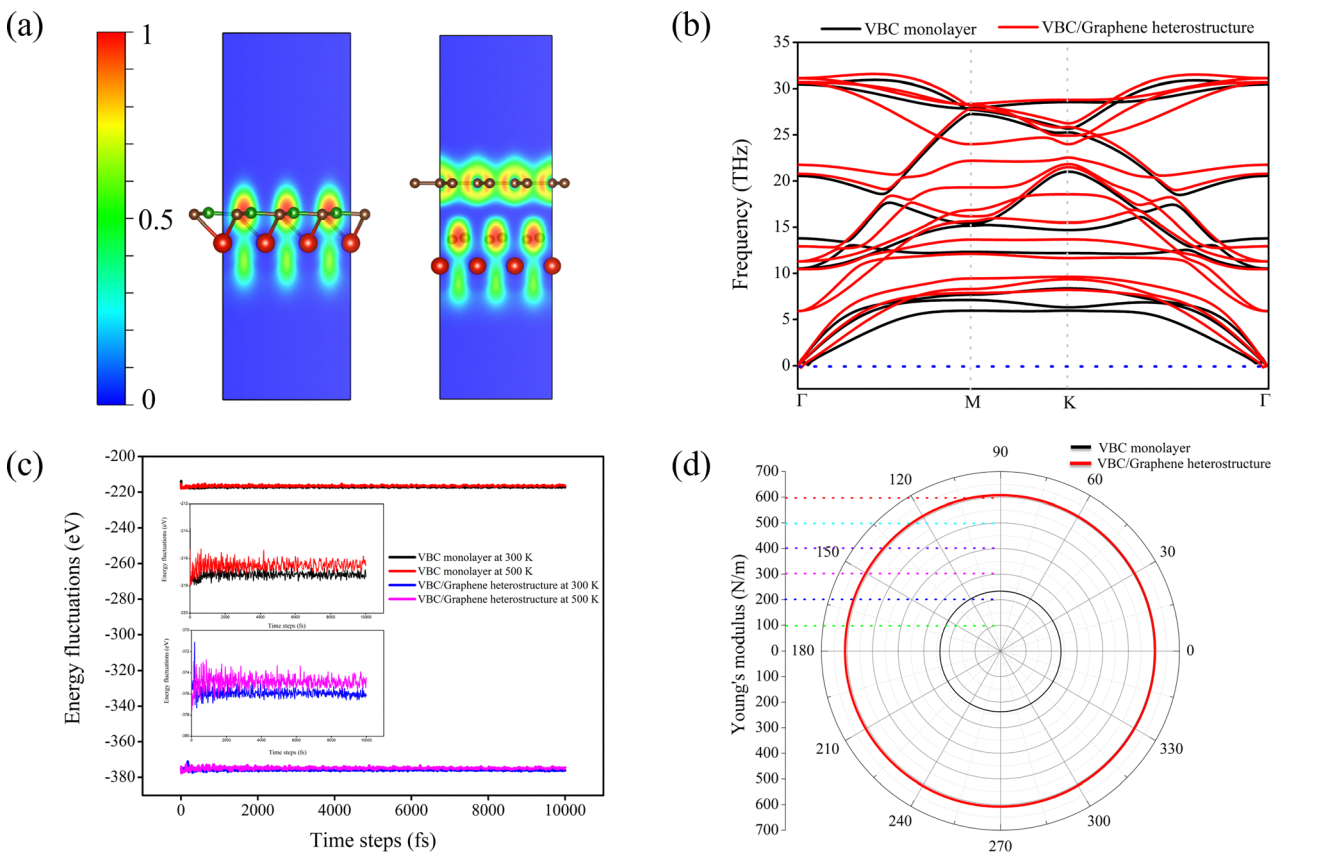

Fig. 2 (a) ELF of the pristine and heterostructure of the VBC monolayer. (b) Dynamic, (c) thermal and (d) mechanical stability of both the pristine and heterostructure of the VBC monolayer.

The work function is a fundamental surface property that characterizes the minimum energy required to extract an electron from the Fermi level of a material to the vacuum level far away from its surface. In the case of two-dimensional materials, the work function can be obtained by first converging the vacuum spacing in slab calculations, such that the local electrostatic potential reaches a constant maximum between the periodic replicas, which represents the vacuum level. The difference between this vacuum level and the Fermi level yields the work function.[68] For the VBC monolayer and VBC/graphene heterostructure, our first-principles calculations predict work functions of 4.80 eV and 4.79 eV, as shown in Fig. S2, which is comparable to that of other 2D reported anode material such as graphene ($\sim$4.6 eV).[69] This moderate value suggests good electron emission characteristics and strong interfacial compatibility with electrolytes, further supporting its potential as an efficient anode material for LIBs.

3.2. Stability

After optimising the atomic structure of the VBC monolayer and the VBC/graphene heterostructure, we systematically investigated their stability, including dynamic, thermal and mechanical stability, which are essential for practical applications. Fig. 2(b) presents the calculated phonon dispersion of the VBC monolayer and the VBC/graphene heterostructure. It can be clearly observed that no imaginary phonon frequencies (negative modes) appear throughout the entire Brillouin zone. The absence of negative frequencies confirms that the VBC monolayer and the VBC/graphene heterostructure are dynamically stable. The very small negative frequencies observed in the acoustic modes near the Γ point are generally considered numerical artifacts. A similar trend has also been reported in 2D monolayers, supporting that these features are not indicative of dynamical instability.[19,70,71] Furthermore, the highest optical phonon mode reaches $\sim$33 THz, which reflects the strong bonding nature within the lattice. For comparison, this maximum phonon frequency is higher than many reported 2D monolayers such as SnS (9.6 THz), $SiSe_2$ (12.6 THz), and MoS_2 (14.2 THz). The thermodynamic properties of the VBC monolayer and VBC/graphene heterostructure, derived from its phonon spectrum, confirm its structural stability and predict exceptional resilience for battery anode applications. The free energy ($F = E - TS$) determine the thermodynamic stability of a material. As observed, the Gibb's free energy (F) decreases with T and become negative around $\sim 7 \times 10^2$ K for the VBC monolayer and above 8×10^2 K for the VBC/graphene heterostructure, indicating that the material is thermodynamically stable and can be synthesized at temperature exceeding this threshold. Furthermore, the observed behaviour is consistent with temperature variations of entropy and heat capacity at constant volume, C_V (T), as shown in Fig. S3. To evaluate the thermal stability of the VBC monolayer and VBC/graphene heterostructure, AIMD simulations were performed at 300 K and 500 K with a time duration of 10 ps (10 000 fs), as illustrated in Fig. 2(c). The total energy fluctuations remain nearly constant with only minor oscillations around the mean values at both temperatures. At 300 K, the energy curve is stable with negligible fluctuations, while at 500 K, slightly larger but still bounded fluctuations are observed. Importantly, no structural distortions or bond breakages were observed during simulations, indicating that the VBC monolayer and VBC/graphene heterostructure preserve its structural integrity even under elevated thermal conditions.

The mechanical stability of the VBC monolayer and VBC/graphene heterostructure was evaluated using the calculated elastic constants C_{ij}. For hexagonal symmetry, one two independent in-plane elastic constants, C_{11} and C_{12}, are required, while the shear modulus can be obtained from the relationship $C_{66} = (C_{11} - C_{12})/2$. The obtained elastic constants can be represented in the stiffness matrix using Voigt notation, which describe the in-plane mechanical response of the VBC monolayer and VBC/graphene heterostructure as:

$$C_{ij} = \begin{bmatrix} C_{11} & C_{21} & 0 \\ C_{12} & C_{22} & 0 \\ 0 & 0 & (C_{11} - C_{12})/2 \end{bmatrix} \quad (4)$$

The calculated elastic constant values are C_{11} = 233.71/620.58 N m^{-1}, C_{12} = 29.76/119.13 N m^{-1}, and C_{66} = 101.92/250.72 N m^{-1} for the VBC monolayer and VBC/graphene heterostructure. The Born–Hung stability criteria for 2D materials require that $C_{11} > 0$, $C_{66} > 0$, ${C_{11}}^2 > {C_{12}}^2$. These conditions are fully satisfied by the present results, confirming that the VBC monolayer and VBC/graphene heterostructure are mechanically stable. The directional dependence of the elastic response was further examined by calculating the variation of Young's modulus and Poisson's ratio as a function of the in-plane orientation, based on the obtained elastic stiffness constants.[70] Their analytical forms are defined as:

$$Y(\theta) = \frac{C_{11}C_{22} - {C_{12}}^2}{C_{11}S^4 + C_{22}C^4 + \left[\frac{C_{11}C_{22} - {C_{12}}^2}{C_{66}} - 2C_{12}\right]C^2S^2} \quad (5)$$

$$\nu(\theta) = \frac{C_{12}(S^4 + C^4) - \left[C_{11} + C_{12} - \frac{C_{11}C_{22} - {C_{12}}^2}{C_{66}}\right]C^2S^2}{C_{11}S^4 + C_{22}C^4 + \left[\frac{C_{11}C_{22} - {C_{12}}^2}{C_{66}} - 2C_{12}\right]C^2S^2} \quad (6)$$

where C_{11}, C_{12}, and C_{66} are the elastic constants and $S = \sin(\theta)$ and $C = \cos(\theta)$. The calculated Young's modulus values are 229.92 N m^{-1} for the VBC monolayer and 597.58 N m^{-1} for the VBC/graphene heterostructure, and their polar plots of $Y(\theta)$ are shown in Fig. 2(d). The calculated Poisson's ratios (ν) are 0.127 for the VBC monolayer and 0.192 for the VBC/graphene heterostructure, as shown in Fig. S4, both of which are positive, satisfying the Born stability criteria. Furthermore, the low Poisson's ratio indicates minimal lateral contraction under tensile strain, which further highlights the structural rigidity. Notably, the obtained Poisson's ratio lies within the range commonly reported for conventional materials.[72] Overall, these results demonstrate that VBC exhibits excellent mechanical stability and notable stiffness, ensuring its suitability for applications where mechanical robustness is essential.

3.3. Li adsorption and diffusion

To evaluate the potential of the VBC monolayer and VBC/graphene heterostructure as an anode material for Li-ion batteries, we systematically studied Li adsorption at different adsorption sites. Owing to the lattice symmetry of the VBC monolayer, three representative adsorption sites were considered, namely the B-site (top of the boron atom), C-site (top of the carbon atom), and V-site (top of the vanadium atom), as illustrated in Fig. 3. The calculated adsorption energies of Li on the VBC monolayer and VBC/graphene heterostructure are all negative, with values of −0.70/−1.68 eV (B-site), −0.74/−1.37 eV (C-site), and −1.21/−2.21 eV (V-site). These negative adsorption energies confirm that Li atoms can stably adsorb on the VBC monolayer and VBC/graphene heterostructure rather than clustering into metallic Li. Among these sites, the V-site exhibits the strongest adsorption interaction (−1.21/−2.21 eV), suggesting it as the most favourable adsorption site for Li storage. In addition, the Bader charge analysis reveals significant charge transfer from Li atoms to the VBC monolayer and VBC/graphene heterostructure, with transferred charges of 0.90/0.71 $|e|$ (V-site), 0.86/0.67 $|e|$ (C-site), and 0.89/0.68 $|e|$ (B-site). This considerable charge transfer from Li to the VBC monolayer and VBC/graphene heterostructure confirms strong adsorption energy, which is highly beneficial for electrochemical activity. Furthermore, the electronic characteristics of electrode materials play a crucial role in determining their suitability for rechargeable batteries, since fast electron transport ensures efficient charging/discharging. To explore this, we studied the density of states (DOS) (Fig. S5), band structure (Fig. S6), and charge density difference of the Li-adsorbed VBC monolayer and VBC/graphene heterostructure, as shown in Fig. 4. Upon Li adsorption, the total DOS shows additional contribution near the Fermi level, primarily arising from the hybridization between Li-2s states and the host V-d states, as shown Fig. S5. The presence of continues states at the Fermi level confirms that the metallic nature of the VBC monolayer and VBC/graphene heterostructure is preserved after Li adsorption. The band structure further confirms multiple band crossings at the Fermi level, as shown Fig. S6, ensuring robust electrical conductivity during electrochemical operation. In addition, the charge density difference ($\Delta\rho$) plots (Fig. 4a and b) illustrate the charge redistribution upon Li adsorption. The cyan regions surrounding the Li atom represent charge depletion, while the yellow regions near the VBC lattice represent charge accumulation. This indicates that Li donates its valence electron to the host monolayer and VBC/graphene heterostructure. Quantitative Bader analysis further confirms a significant charge transfer at a higher adsorption energy site of ∼0.90/0.71 $|e|$ from Li to the VBC sheet and VBC/graphene heterostructure. Such strong charge transfer facilitates the stabilization of adsorbed Li atoms and improves the electrochemical activity of the system.

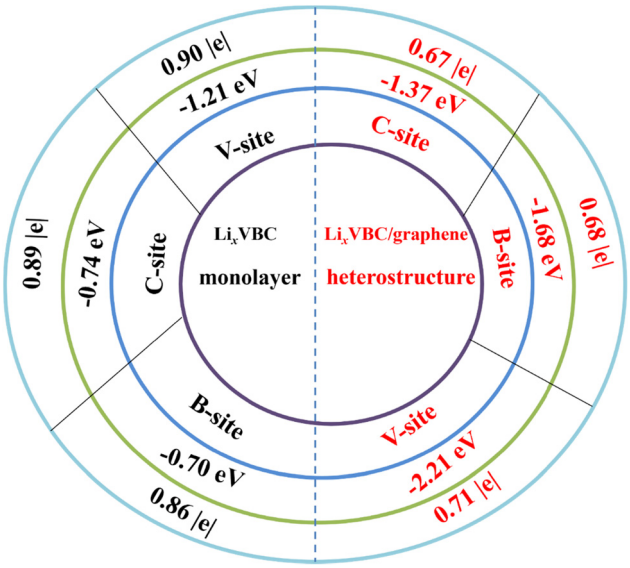

Fig. 3 Adsorption energies and the charge transfer rate at different stable adsorption sites of the VBC monolayer and VBC/graphene heterostructure.

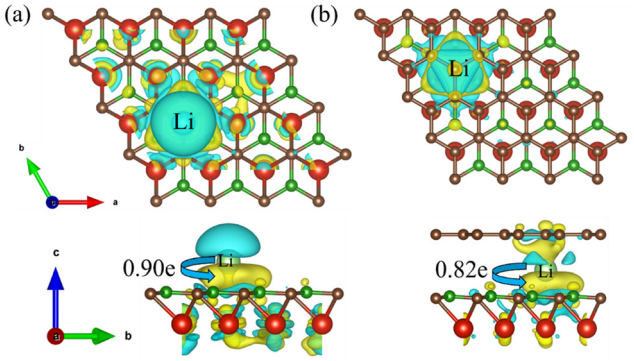

Fig. 4 Charge density differences map of the (a) VBC monolayer and (b) VBC/graphene heterostructure at a high adsorption site.

The rate performance of Li-ion batteries is closely linked to the mobility of Li ions within the electrode material, which is primarily governed by the diffusion energy barrier. A lower diffusion barrier facilitates faster Li migration, enabling rapid charge/discharge cycles. To explore this, we employed the CI-NEB method to calculate Li-ion diffusion barriers along different pathways on the VBC monolayer and VBC/graphene heterostructure surfaces, as illustrated in Fig. 5. Three possible diffusion pathways between adjacent stable adsorption sites were considered: Path V–B, Path V–C, and Path C–B. The calculated diffusion energy profiles of the VBC monolayer and the VBC/graphene heterostructure are shown in Fig. 5(d) and (e), respectively. Among these, the C–B path exhibits the lowest diffusion barrier of ∼0.22/0.31 eV, indicating highly favourable Li mobility along this path. In comparison, the V–C path shows a moderate barrier of ∼0.41/0.84 eV, while the V–B path presents the highest barrier of ∼0.63/0.54 eV. The increase in the diffusion energy barrier of the heterostructure at certain sites arises from the presence of the graphene layer, which modifies the local atomic environment at the interface and strengthens Li interactions at specific adsorption sites. In addition, the interface provides a more confined pathway

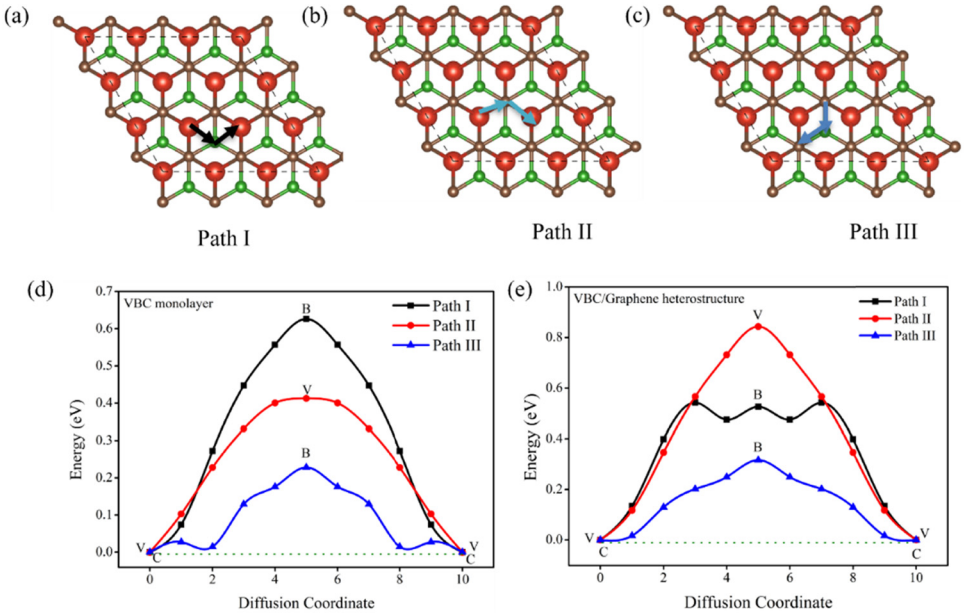

Fig. 5 (a–c) Li migration paths on the VBC surface, and (d, e) diffusion energy barriers of Li on the VBC monolayer and VBC/graphene heterostructure, respectively.

compared to the open surface of the monolayer, further contributing to the higher barrier. Moreover, the graphene layer enhances electronic conductivity and structure stability, which are beneficial for overall electrochemical performance. The calculated energy barriers within the typical range reported for 2D anode materials (~0.2–1.0 eV), as shown in Table 2. Notably, the diffusion barrier along the C–B pathway is remarkably low, and comparable to other reported 2D materials such as graphite anode materials,[73–75] and close to other 2D monolayers, as depicted in Table 2. Such low barrier values highlight the ability of the VBC monolayer and VBC/graphene heterostructure to support rapid Li migration, which is essential for achieving high-rate performance and fast charging in Li-ion batteries.

3.4. Top/bottom Li adsorption potential and storage capacity

We next evaluated Li uptake on the VBC monolayer and VBC/graphene heterostructure by progressively increasing the Li concentration (x = 0 → 4) and calculating the corresponding adsorption energies. As shown in Fig. 6(a), all computed adsorption energies are negative across the examined concentration range, indicating that Li atoms remain thermodynamically bound to the VBC monolayer surface rather than aggregating into a bulk metal. The adsorption energy weakens monotonically with increasing Li content from low x = 0.11 to high concentration x = 4 (36 Li ions). The adsorption energy gradually decreases from −1.21 eV to −0.39 eV with increasing Li coverage, and this trend is attributed to the increasing electrostatic repulsion among adsorbed Li ions and the gradual reduction of the Li–host interaction as adsorption sites becomes progressively occupied. We found that strongly negative adsorption energies are favorable for stabilizing metal-ion adsorption on the 2D material surface and preventing ion clustering that ensure metal-ion stability.[76,77] Moreover, the observed reduction in adsorption strength at higher Li

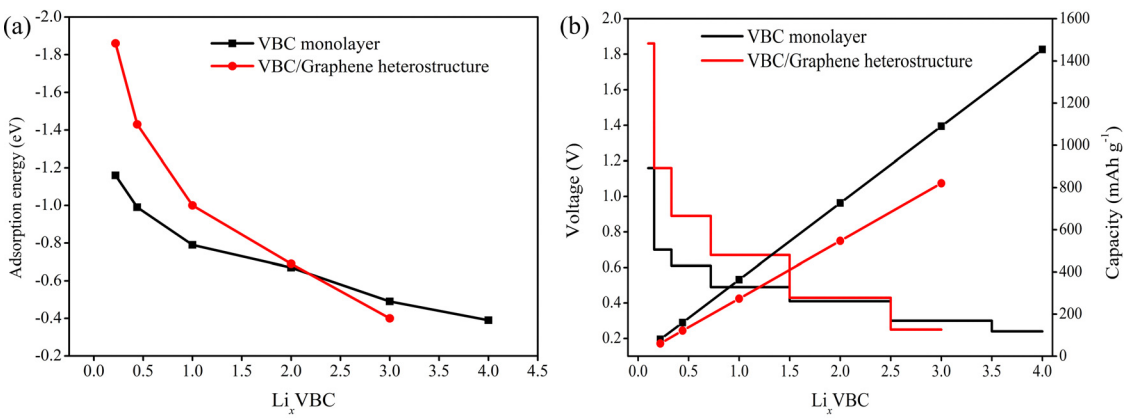

Fig. 6 (a) Adsorption energies and (b) voltage profiles of the VBC monolayer and VBC/graphene heterostructure at different Li concentrations.

concentrations can be advantageous for battery operation, as excessively strong binding may hinder Li diffusion and extraction. Therefore, the adsorption energy of −0.39 eV suggests a reasonable balance between adsorption stability and diffusion kinetics, which is beneficial for reversible electrochemical performance. Furthermore, our results are consistent with those reported for other high-capacity electrode materials that exhibit high Li adsorption content.[10,19,77–79] Importantly, the fully optimized structures at each concentration show no bond breaking or catastrophic structural changes (see inset geometries), confirming that the VBC lattice can tolerate multi-layer Li loading up to the studied maximum concentration. In comparison, the VBC/graphene heterostructure consistently exhibits stronger binding with Li at lower concentrations, as reflected by the more negative adsorption energies (≈ -1.82 eV at $x = 0.22$ compared to −1.15 eV for the monolayer). This enhanced affinity is likely due to the synergistic effect of the heterostructure interface, where graphene provides additional delocalized π-electron density that promotes Li stabilization. However, as the Li content increases, the adsorption energies in the heterostructure decrease more rapidly and eventually converge toward values similar to those of the monolayer around $x \approx 2$. Beyond this point, the heterostructure exhibits slightly weaker binding at high coverage, suggesting that steric hindrance and charge redistribution across the interface limit further enhancement. Overall, the results highlight that the VBC/graphene heterostructure offers a stronger driving force for initial Li uptake, which can be beneficial for fast charging processes, while maintaining structural stability across the examined loading range.

To further evaluate the electrochemical performance of the VBC-based systems, we calculated the average open circuit voltage (OCV) and corresponding theoretical capacity of both the VBC monolayer and the VBC/graphene heterostructure as a function of Li concentration (Li_xVBC, $x = 0 \rightarrow 4$). The OCV is a critical descriptor for anode materials, as efficient Li-ion batteries require low operating voltages at the anode while maintaining sufficiently high voltages at the cathode to maximize the overall cell potential. The lithiation and delithiation process of the anode material is expressed as follows:

$$VBC + xLi^+ + xe^- \rightleftarrows Li_xVBC \quad (7)$$

During the electrochemical process, electrons are transferred through an external circuit to generate an electric current, while Li^+ ions concurrently diffuse through the electrolyte and shuttle between the anode and the cathode to maintain charge balance. The voltage profiles shown in Fig. 6(b) reveal that both the VBC monolayer and VBC/graphene heterostructure systems exhibit a decreasing voltage with increasing Li concentration, which is consistent with the progressive weakening of adsorption strength observed in the adsorption energy results. Specifically, the VBC monolayer shows a gradual voltage drop from ∼1.15 V at low Li coverage to ∼0.23 V at maximum loading ($x = 4$), while the VBC/graphene heterostructure starts at a higher initial voltage (∼1.83 V) and decreases more steeply to ∼0.21 V at $x = 3$. The calculated average voltages are 0.45 V for the VBC monolayer and 0.68 V for the VBC/graphene heterostructure. The calculated average voltages fall within the range suitable for commercial anode materials, such as $LiTiO_2$ (1.5–1.8),[80] and graphite (0.2 V).[81] The relatively high initial voltage (>1.1 V) may influence full-cell performance by reducing the effective cell voltage when paired with a typical cathode. Such higher initial voltages are commonly associated with strong Li binding at the early stages of lithiation and have been reported in several emerging anode materials.[82–86] From a practical perspective, the initial voltage mainly affects the early stage of lithiation and typically decreases rapidly with increasing Li content, leading to stable average operating voltage, as commonly observed in Li-ion electrode materials.[87] Therefore, its impact on the overall full-cell voltage is limited. Moreover, recent studies emphasize that interfacial processes, electrolyte stability, and electrode play a more critical role in determining full-cell performance than the initial lithiation voltage.[88] In addition, the theoretical capacities were derived from the relationship $C = \frac{xF}{M}$, where x is the Li content, F is the Faraday constant, and M is the molar mass of the host. At maximum loading, the VBC monolayer achieves a very high theoretical capacity of ∼1453.36 mAh g^{-1}, while the VBC/graphene heterostructure reaches ∼820 mAh g^{-1}. Both values surpass many conventional anode materials such as graphite (372 mAh g^{-1})[89] and TiO_2 (335 mAh g^{-1}),[90] highlighting the promise of these systems for high-energy-density Li-ion storage.

3.5. Safety

We examined the structural response of the VBC system to lithium insertion, focusing on lattice expansion and volumetric changes, which are key factors influencing the stability of anode materials in rechargeable batteries. Table 1 summarizes

Table 1 Relative change in the lattice parameter and volume of the VBC monolayer and VBC/graphene heterostructure at different Li atom concentrations

System	ΔL (Å)		ΔV (Å^3)	
	Monolayer (%)	Heterostructure (%)	Monolayer (%)	Heterostructure (%)
$Li_{0.11}$VBC/graphene	0.19	0.06	2.24	1.98
Li_1 VBC/graphene	0.52	0.37	4.06	6.84
Li_2 VBC/graphene	1.45	1.74	5.6	9.27
Li_3 VBC/graphene	2.57	2.88	6.73	10.7
Li_4 VBC/graphene	2.62		7.49	

the calculated lattice parameter changes (ΔL) and volume changes (ΔV) for varying lithium concentrations. As the Li content in Li_xVBC increases from x = 0.11 to 4, the lattice parameters show a progressive expansion, ranging from 0.19% to 2.62%. Correspondingly, the system's volume increases from 2.24% to 7.49%, indicating that higher lithium loading leads to more pronounced structural enlargement. For the VBC/graphene heterostructure, the structural response to lithiation was evaluated by examining the variations in the lattice (ΔL) and volume (ΔV) at different lithium concentrations. As the Li content in Li_xVBC/graphene increases from x = 0.11 to 3, a gradual expansion of the lattice is observed. The lattice parameter variation rises from 0.06% at low Li coverage to 2.88% at the highest loading level, while the corresponding volumetric change reaches 10.7% at full lithiation. However, the overall expansion in both the VBC monolayer and the VBC/graphene heterostructure remains moderate and comparable to that of conventional graphite anodes, which typically exhibits ~10%[118] anisotropic volumetric expansion (primarily along the c-axis) upon full lithiation. In this study, the VBC monolayer exhibits lower volume changes, whereas the VBC/graphene heterostructure shows a slightly higher value, but both remain within a similar range to graphite. This restrained expansion implies that the VBC and VBC/graphene heterostructure systems are likely to maintain good mechanical stability during repeated charge–discharge cycles, highlighting their potential for high-cycling performance in lithium-ion applications. Overall, the data indicate that the VBC monolayer and VBC/graphene heterostructure accommodate lithium insertion efficiently, with limited structural distortion, supporting its suitability as stable anode materials.

Table 2 Comparative analysis of specific capacity, ion-diffusion barriers, and open-circuit voltage (OCV) for prospective anode materials in Li-ion batteries

Materials	Voltage (V)	Energy barrier (eV)	Capacity (mAh g^{-1})	Ref.
C_3B	0.52	0.40	714	91
SiN_3	0.43	0.025	1146	92
VC_4	0.52	0.18	1353	36
SW-BC_3	0.48	0.33	1287	93
PC_5	0.46	0.47	1251.7	94
PC_6	0.92	0.44	1235.9	94
C_6BN	0.12	0.47	830	95
B_2N	1.07	0.47	1082	96
V_4C_3	0.38	0.048	223	97
V_2C_2	0.46	0.89	412	98
WC_4	0.65	0.55	577	99
V_2C	0.42	0.045	941	100
BC_3	0.48	0.34	1144	93
F, Si-CTFs	2.57	0.078	462	101
ZrB_2C_2	0.42	0.51	1028.02	102
$B_3C_2N_3$	0.09	—	1334	103
AsB	0.39	0.34	555.84	104
HOT-graphene	0.26	0.51	744	105
0D-BC_3	0.14	0.61	1430	106
Cu_2N	0.3–0.6	0.0051	1139.6	107
$Si_6O_3H_6$	0.66	0.34	1129.18	108
HB	0.37	0.74	1134	109
WS_2/graphene	0.18	0.27	588.16	110
BC_2N/graphene	0.32	0.073	691	111
Silicene/graphene	1.07	0.36–0.40	487	112
VS_2/graphene	—	0.2	569	47
Gr/blueP/MoS_2	0.26	0.066–0.22	818	113
MXenes/graphene	0.27	0.2–0.5	383	114
BN/TiS_2	1.02	0.33	392	115
MoS_2/TaS_2	0.8	—	589	116
Nb_2Se_2C	0.80	0.26	454.75	117
VBC	0.45	0.22	1453.36	This study
VBC/graphene	0.68	0.31	820.60	This study

To further assess the dynamic stability of the VBC system under lithiation, AIMD simulations were performed at 300 K for a duration of 10 000 fs time steps, as shown in Fig. 7(a). Throughout the simulation, the total energy exhibits only minor fluctuations around an equilibrium value, with no evidence of abrupt changes or instability. This indicates that the lithiated VBC maintains structural robustness under ambient thermal conditions. The snapshots of the atomic configuration before and after the AIMD run further confirm the stability of the system. In addition, the AIMD simulations of the VBC/graphene heterostructure are shown in Fig. S7. The overall lattice framework of the VBC monolayer and VBC/graphene heterostructure remains preserved, with no bond breaking or significant distortions observed. The inserted Li atoms exhibit only slight oscillations around their adsorption sites, which is characteristic of thermally stable intercalated systems. Importantly, the absence of major deformations or structural collapse during the simulation suggests that the VBC framework can endure the repeated processes of Li-ion intercalation and extraction without undergoing substantial degradation. These results highlight the intrinsic thermal resilience of the VBC monolayer and VBC/graphene heterostructure at room temperature, even under full lithiation conditions. Such stability under dynamic simulation conditions strongly supports its potential application as an anode material, since minimal structural perturbation under operational environments is crucial for ensuring long-term cycling stability in LIBs.

To examine the nature of chemical bonding in the VBC monolayer and VBC/graphene heterostructure, the electron localization function (ELF) was employed. ELF mapping provides insight into regions of electron accumulation, allowing a detailed assessment of how electrons are distributed around the incorporated Li atoms. This analysis offers a clear understanding of how alkali-metal adsorption modifies the local bonding environment and influences the overall electronic characteristics of the material. Fig. 7c and d show the charge distribution of the systems after Li was adsorbed onto the surfaces, providing insight into the ELF characteristics of both the VBC monolayer and the VBC/graphene heterostructure. Our analysis indicates that charge transfer predominantly takes place between the adsorbed Li^+ ions and the VBC monolayer as well as the VBC/graphene heterostructure. Under full lithiation, the emergence of pronounced yellow and green ELF regions reflects the development of substantial electron density around the adsorption sites. The accumulation of these electron clouds points to improved electronic transport within the VBC monolayer as well as the VBC/graphene heterostructure, confirming its robust metallic behaviour and the stability of the adsorption layers.

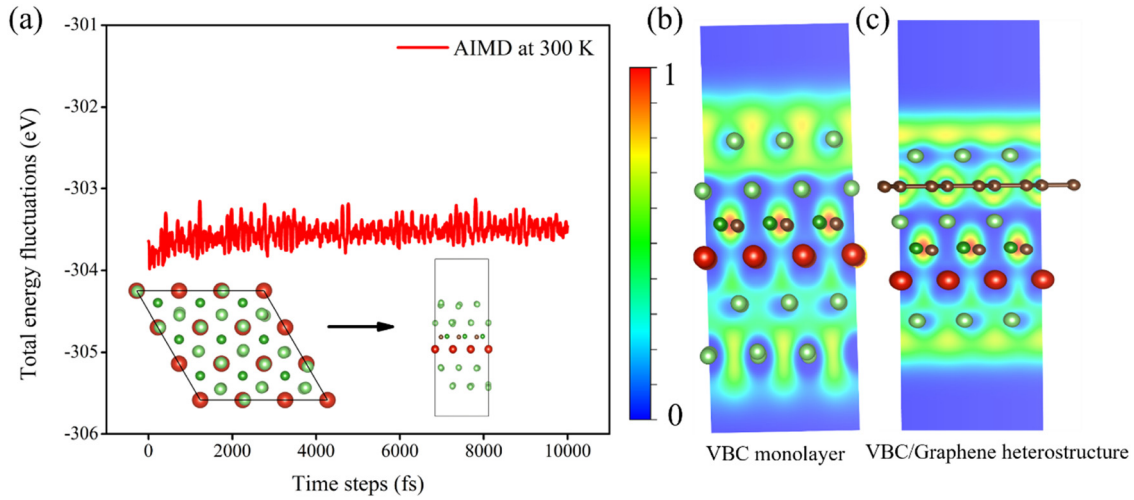

Fig. 7 (a) AIMD simulations and (b) and (c) ELF map of the fully lithiated VBC monolayer and VBC/graphene heterostructure. The ELF range: red (ELF > 0.5) indicates covalent bonding, green (ELF = 0.5) reflects metallic character, and blue (ELF < 0.5) corresponds to ionic bonding regions.

3.6. Electrolyte wettability

Wettability plays a crucial role in determining the compatibility between an electrode surface and the electrolyte, as it governs how effectively the liquid phase can spread, penetrate, and establish intimate interfacial contact with the active material.[119] Proper wetting ensures uniform ion transport pathways and promotes stable interfacial reactions, whereas insufficient or uneven wettability can lead to irregular charge distribution, unstable solid electrolyte interface (SEI) formation, and ultimately degraded cycling performance. Therefore, evaluating the stability of the SEI formed on the VBC monolayer and VBC/graphene heterostructure in contact with a commercial electrolyte is essential.[120] As illustrated in Fig. S7, lithium hexafluorophosphate ($LiPF_6$) was adsorbed at the energetically favorable site on both the VBC monolayer and the VBC/graphene heterostructure. $LiPF_6$ is commonly used as the main conductive lithium salt dissolved in organic solvent mixtures of high dielectric constant cyclic carbonates. Wettability is commonly assessed through the adsorption energy of an electrolyte species on the electrode surface. The adsorption energy was calculated using the following equation: $E_{ad} = E_{adsorbate+VBC} - E_{VBC} - E_{adsorbate}$, where $E_{adsorbate}$ represents the energy of an individual electrolyte molecule. The calculated adsorption energy of the VBC monolayer is −0.47 eV and −2.07 eV for the VBC/graphene heterostructure. The adsorption energies of the selected metal salt on the VBC monolayer and the VBC/graphene heterostructure were found to be comparable or higher than those reported for graphene (0.54–0.87 eV) and silicon pentanitride (0.12–0.67 eV).[121] The more negative adsorption energy indicates stronger electrolyte–surface interactions, which is beneficial for improving electrolyte wettability and interfacial contact.[122] However, it is also important to note that excessively strong adsorption may also enhance interfacial electrolyte decomposition, which can influence solid–electrolyte (SEI) formation. Overall, the $LiPF_6$ adsorption behavior suggests good wettability that supports stable interfacial chemistry and contributes to the overall safety of the cell.

4. Conclusions

In summary, first-principles calculations establish the VBC monolayer and VBC/graphene heterostructure as highly promising anode materials for next-generation lithium-ion batteries. Both systems demonstrate excellent thermodynamic, mechanical, and dynamical stability, confirming their potential for experimental realization. Their intrinsic metallic character, preserved throughout lithiation, ensures superior electronic conductivity, while the ultrahigh theoretical capacities of 1453.36 mAh g^{-1} for the VBC monolayer and 820.60 mAh g^{-1} for the VBC/graphene heterostructure. Minimal lattice variation under full lithiation further confirms the structural resilience essential for long-term cycling stability. The favourable adsorption energies of $LiPF_6$ on both VBC-based electrodes indicate good electrolyte wettability, supporting stable interfacial chemistry and reliable SEI formation. These results establish the VBC monolayer and VBC/graphene heterostructure as promising anode materials for LIBs.

Conflicts of interest

The authors declare that they have no known competing financial interests or personal relationships that could have appeared to influence the work reported in this paper.

Data availability

The supporting data have been provided as part of the supplementary information (SI) (Fig. S1 to S8). The supplementary information includes K-point value and total-energy convergence test, work function, thermodynamic quantities, Poisson's ratio, density of states (DOS), electronic band structure, AIMD

simulations, and adsorption configuration of $LiPF_6$. See DOI: https://doi.org/10.1039/d6ma00263c.

Acknowledgements

The authors would like to acknowledge the support from the School of Biological and Chemical Sciences at the University of Galway, Ireland. In addition, we would like to extend our gratitude to the Irish Centre for High End Computing (ICHEC) for providing the computational resources under project ID p201052.

References

1 P. A. Owusu and S. Asumadu-Sarkodie, *Cogent Eng.*, 2016, **3**, 1167990.
2 R. G. Miller and S. R. Sorrell, *Philos. Trans. R. Soc., A*, 2014, **372**, 20130179.
3 J. B. Goodenough and Y. Kim, *Chem. Mater.*, 2010, **22**, 587–603.
4 N. Khossossi, A. Banerjee, Y. Benhouria, I. Essaoudi, A. Ainane and R. Ahuja, *Phys. Chem. Chem. Phys.*, 2019, **21**, 18328–18337.
5 D. Larcher and J.-M. Tarascon, *Nat. Chem.*, 2015, **7**, 19–29.
6 S. Hy, H. Liu, M. Zhang, D. Qian, B.-J. Hwang and Y. S. Meng, *Energy Environ. Sci.*, 2016, **9**, 1931–1954.
7 S. Megahed and W. Ebner, *J. Power Sources*, 1995, **54**, 155–162.
8 B. Dunn, H. Kamath and J.-M. Tarascon, *Science*, 2011, **334**, 928–935.
9 A. Manthiram, *J. Phys. Chem. Lett.*, 2011, **2**, 176–184.
10 S. Karmakar, C. Chowdhury and A. Datta, *J. Phys. Chem. C*, 2016, **120**, 14522–14530.
11 D. Chodvadiya, U. Jha, P. Śpiewak, K. J. Kurzydłowski and P. K. Jha, *Appl. Surf. Sci.*, 2022, **593**, 153424.
12 K.-S. Chen, I. Balla, N. S. Luu and M. C. Hersam, *ACS Energy Lett.*, 2017, **2**, 2026–2034.
13 Q. Peng, Z. Wang, B. Sa, B. Wu and Z. Sun, *ACS Appl. Mater. Interfaces*, 2016, **8**, 13449–13457.
14 B. Liu, X. Sun, Z. Liao, X. Lu, L. Zhang and G.-P. Hao, *Sci. Rep.*, 2021, **11**, 5633.
15 E. M. Siriwardane, I. Demiroglu, C. Sevik and D. Çakır, *ACS Appl. Energy Mater.*, 2019, **2**, 1251–1258.
16 M. Yoshio, H. Wang and K. Fukuda, *Angew. Chem., Int. Ed.*, 2003, **42**, 4203–4206.
17 M. Makaremi, B. Mortazavi, T. Rabczuk, G. A. Ozin and C. V. Singh, *ACS Appl. Nano Mater.*, 2018, **2**, 127–135.
18 B. Mortazavi, A. Dianat, G. Cuniberti and T. Rabczuk, *Electrochim. Acta*, 2016, **213**, 865–870.
19 P. Patel, S. Patel, D. Chodvadiya, M. H. Dalsaniya, D. Kurzydłowski and P. K. Jha, *ACS Appl. Nano Mater.*, 2023, **6**, 2103–2115.
20 U. Kasavajjula, C. Wang and A. J. Appleby, *J. Power Sources*, 2007, **163**, 1003–1039.
21 C. Tan, X. Cao, X.-J. Wu, Q. He, J. Yang, X. Zhang, J. Chen, W. Zhao, S. Han and G.-H. Nam, *Chem. Rev.*, 2017, **117**, 6225–6331.
22 H. Lin, R. Jin, S. Zhu and Y. Huang, *Appl. Surf. Sci.*, 2020, **505**, 144518.
23 Z. Xiao, R. Wang, D. Jiang, Z. Qian, Y. Li, K. Yang, Y. Sun, Z. Zeng and F. Wu, *ACS Appl. Energy Mater.*, 2021, **4**, 7440–7461.
24 H. Xu, H. Chen and C. Gao, *ACS Mater. Lett.*, 2021, **3**, 1221–1237.
25 D. Rao, L. Zhang, Z. Meng, X. Zhang, Y. Wang, G. Qiao, X. Shen, H. Xia, J. Liu and R. Lu, *J. Mater. Chem. A*, 2017, **5**, 2328–2338.
26 S. Mukherjee and G. Singh, *ACS Appl. Energy Mater.*, 2019, **2**, 932–955.
27 Y. Xie, Y. Dall'Agnese, M. Naguib, Y. Gogotsi, M. W. Barsoum, H. L. Zhuang and P. R. Kent, *ACS Nano*, 2014, **8**, 9606–9615.
28 K. Fan, Y. Ying, X. Li, X. Luo and H. Huang, *J. Phys. Chem. C*, 2019, **123**, 18207–18214.
29 V. V. Kulish, O. I. Malyi, C. Persson and P. Wu, *Phys. Chem. Chem. Phys.*, 2015, **17**, 13921–13928.
30 J. Jia, B. Li, S. Duan, Z. Cui and H. Gao, *Nanoscale*, 2019, **11**, 20307–20314.
31 E. Lee and K. A. Persson, *Nano Lett.*, 2012, **12**, 4624–4628.
32 F. J. Sonia, M. K. Jangid, B. Ananthoju, M. Aslam, P. Johari and A. Mukhopadhyay, *J. Mater. Chem. A*, 2017, **5**, 8662–8679.
33 J. Ma, C. Yang, X. Ma, S. Liu, J. Yang, L. Xu, J. Gao, R. Quhe, X. Sun and J. Yang, *Nanoscale*, 2021, **13**, 12521–12533.
34 Y. Liu, X. Zhang, C. Li, N. Gao and H. Li, *Colloids Surf., A*, 2024, **697**, 134455.
35 Q. Tang, Z. Zhou and P. Shen, *J. Am. Chem. Soc.*, 2012, **134**, 16909–16916.
36 Q. Peng, J. Rehman, M. K. Butt, D. Wang, L. Tao, A. M. Tighezza and J. Dai, *J. Energy Storage*, 2024, **95**, 112591.
37 M. Ramezanzadeh, R. Ghamarpoor, A. Dashan, A. Fallah, S. Soleimani and B. Ramezanzadeh, *Adv. Compos. Hybrid Mater.*, 2025, **8**, 269.
38 N. Kumar, H. Singh, M. Khatri and N. Bhardwaj, Age of MXenes, *Fundamentals and Artificial Intelligence: Machine Learning Interventions*, ACS Publications, 2023, vol. 1, pp. 1–25.
39 D. Wang, Y. Liu, X. Meng, Y. Wei, Y. Zhao, Q. Pang and G. Chen, *J. Mater. Chem. A*, 2017, **5**, 21370–21377.
40 Y. Dong, Z. Tang, P. Liang, H. Wan, H. Wang, L. Wang, H. Shu and D. Chao, *J. Colloid Interface Sci.*, 2021, **593**, 51–58.
41 H. I. Gunnarsson, N. Ashraf and Y. Abghoui, *Sustainable Energy Fuels*, 2025, **9**(11), 3068–3077.
42 H. Junfeng, M. Tabish, S. Ajmal, A. Kumar, J. Guo, M. M. Alam and G. Yasin, *Small Methods*, 2025, 2500208.
43 J. Mei, T. Liao and Z. Sun, *Energy Environ. Mater.*, 2022, **5**, 115–132.
44 S. Wang, S. Zhao, X. Guo and G. Wang, *Adv. Energy Mater.*, 2022, **12**, 2100864.
45 J. Wang, B. Wang and B. Lu, *Adv. Energy Mater.*, 2020, **10**, 2000884.

46 H. Liu, X. Chen, L. Deng, X. Su, K. Guo and Z. Zhu, *Electrochim. Acta*, 2016, **206**, 184–191.
47 N. S. Mikhaleva, M. A. Visotin, A. A. Kuzubov and Z. I. Popov, *J. Phys. Chem. C*, 2017, **121**, 24179–24184.
48 X. He, A. Tang, Y. Li, Y. Zhang, W. Chen and S. Huang, *Appl. Surf. Sci.*, 2021, **563**, 150269.
49 P. P. Dinda and S. Meena, *J. Phys.: Condens. Matter*, 2021, **33**, 175001.
50 J. Hafner, *J. Comput. Chem.*, 2008, **29**, 2044–2078.
51 J. P. Perdew, K. Burke and M. Ernzerhof, *Phys. Rev. Lett.*, 1996, **77**, 3865.
52 J. Heyd, G. E. Scuseria and M. Ernzerhof, *J. Chem. Phys.*, 2003, **118**, 8207–8215.
53 S. Grimme, J. Antony, S. Ehrlich and H. Krieg, *J. Chem. Phys.*, 2010, 132.
54 S. Grimme, S. Ehrlich and L. Goerigk, *J. Comput. Chem.*, 2011, **32**, 1456–1465.
55 W. Tang, E. Sanville and G. Henkelman, *J. Phys.: Condens. Matter*, 2009, **21**, 084204.
56 E. Sanville, S. D. Kenny, R. Smith and G. Henkelman, *J. Comput. Chem.*, 2007, **28**, 899–908.
57 X. Gonze and C. Lee, *Phys. Rev. B:Condens. Matter Mater. Phys.*, 1997, **55**, 10355.
58 A. Togo and I. Tanaka, *Scr. Mater.*, 2015, **108**, 1–5.
59 G. J. Martyna, M. L. Klein and M. Tuckerman, *J. Chem. Phys.*, 1992, **97**, 2635–2643.
60 G. Henkelman, B. P. Uberuaga and H. Jónsson, *J. Chem. Phys.*, 2000, **113**, 9901–9904.
61 L. Ali, J. Rehman and C.-W. Zhou, *J. Phys. Chem. Solids*, 2025, **207**, 112940.
62 L. Ali and C.-W. Zhou, *J. Mater. Sci.*, 2025, **60**, 24424–24438.
63 B. C. Revard, W. W. Tipton, A. Yesypenko and R. G. Hennig, *Phys. Rev. B*, 2016, **93**, 054117.
64 H. Ding, S. S. Dwaraknath, L. Garten, P. Ndione, D. Ginley and K. A. Persson, *ACS Appl. Mater. Interfaces*, 2016, **8**, 13086–13093.
65 K. Choudhary, K. F. Garrity, S. T. Hartman, G. Pilania and F. Tavazza, *Phys. Rev. Mater.*, 2023, **7**, 014009.
66 A. K. Geim and I. V. Grigorieva, *Nature*, 2013, **499**, 419–425.
67 Q. Peng, J. Rehman, M. K. Butt, L. Tao, U. Younis, A. El-marghany, M. B. Hanif and Z. Li, *Mater. Today Chem.*, 2025, **43**, 102465.
68 J. Paul, A. Singh, Z. Dong, H. Zhuang, B. Revard, B. Rijal, M. Ashton, A. Linscheid, M. Blonsky and D. Gluhovic, *J. Phys.: Condens. Matter*, 2017, **29**, 473001.
69 S. Naghdi, G. Sanchez-Arriaga and K. Y. Rhee, *J. Alloys Compd.*, 2019, **805**, 1117–1134.
70 B. D. Aparicio-Huacarpuma, E. Marinho, W. F. Giozza, A. M. Silva, C. Kenfack-Sadem, A. C. Dias and L. A. Ribeiro, *Nanoscale*, 2025, **17**, 16003–16011.
71 B. Özdamar, G. Özbal, M. N. Çınar, K. Sevim, G. Kurt, B. Kaya and H. Sevinçli, *Phys. Rev. B*, 2018, **98**, 045431.
72 G. N. Greaves, A. L. Greer, R. S. Lakes and T. Rouxel, *Nat. Mater.*, 2011, **10**, 823–837.
73 J. Hu, Y. Liu, N. Liu, J. Li and C. Ouyang, *Phys. Chem. Chem. Phys.*, 2020, **22**, 3281–3289.
74 K. Toyoura, Y. Koyama, A. Kuwabara, F. Oba and I. Tanaka, *Phys. Rev. B:Condens. Matter Mater. Phys.*, 2008, **78**, 214303.
75 X. Fan, W. Zheng and J.-L. Kuo, *ACS Appl. Mater. Interfaces*, 2012, **4**, 2432–2438.
76 F. Mollaamin, *BMC Chem.*, 2025, **19**, 233.
77 M. K. Masood, J. Wang, J. Song and Y. Liu, *Appl. Surf. Sci.*, 2024, **652**, 159301.
78 X. Fu, X. Zhang, X. He, Z. He, L. Ma, H. Wang, J. Rong, H. Li and X. Yu, *J. Power Sources*, 2026, **667**, 239218.
79 X. Zhu, K. Wu, B. Ma, X. Wang, D. Kong and Y. Wang, *Sci. Rep.*, 2025, **15**, 15902.
80 Z. Yang, D. Choi, S. Kerisit, K. M. Rosso, D. Wang, J. Zhang, G. Graff and J. Liu, *J. Power Sources*, 2009, **192**, 588–598.
81 H. Zheng, K. Jiang, T. Abe and Z. Ogumi, *Carbon*, 2006, **44**, 203–210.
82 C. Tang, M. Zhang, K. Zhang and J. Gong, *Appl. Surf. Sci.*, 2021, **564**, 150468.
83 X. Zhang, X. Fu, J. Chen, X. Yu, J. Chen, K. Chen, R. Gao, J. Rong and H. Li, *Colloids Surf., A*, 2026, 139632.
84 Z. Wang, J. Jiang, H. Tang, H. Guo, W. Wang, Z. Zhuo and N. Lu, *J. Energy Storage*, 2026, **141**, 119223.
85 F. Ghorbani Shadpey, M. Soleimani and M. Pourfath, *ACS Omega*, 2026, **11**(14), 22007–22016.
86 R. Hu, C.-S. Liu and X.-J. Ye, *J. Power Sources*, 2026, **667**, 239223.
87 N. Nitta, F. Wu, J. T. Lee and G. Yushin, *Mater. Today*, 2015, **18**, 252–264.
88 L. Ma, Y. Dong, N. Li, W. Yan, S. Ma, Y. Fang, Y. Li, L. Xu, C. Liu and S. Chen, *etransportation*, 2024, **20**, 100312.
89 Y. Wu, C. Jiang, C. Wan and E. Tsuchida, *Electrochem. Commun.*, 2000, **2**, 272–275.
90 W. Yan, J. Wang, Q. Hu, J. Fu, M. K. Albolkany, T. Zhang, X. Lu, F. Ye and B. Liu, *Nano Res.*, 2024, **17**, 2655–2662.
91 Y. Liu, V. I. Artyukhov, M. Liu, A. R. Harutyunyan and B. I. Yakobson, *J. Phys. Chem. Lett.*, 2013, **4**, 1737–1742.
92 M. K. Butt, J. Rehman, Z. Yang, A. El-marghany, Z. Li and M. F. Shibl, *J. Energy Storage*, 2024, **93**, 112290.
93 S. Thomas, A. K. Madam and M. A. Zaeem, *J. Phys. Chem. C*, 2020, **124**, 5910–5919.
94 K. Fan, Y. Ying, X. Luo and H. Huang, *Phys. Chem. Chem. Phys.*, 2020, **22**, 16665–16671.
95 M. K. Butt, F. Ye, K. Long, A. El-marghany, Y. Zhao, J. Rehman and Z.-P. Li, *J. Power Sources*, 2025, **644**, 237119.
96 X. Zhou, X. Chen, C. Shu, Y. Huang, B. Xiao, W. Zhang and L. Wang, *ACS Appl. Mater. Interfaces*, 2021, **13**, 41169–41181.
97 Q. Peng, J. Rehman, K. Eid, A. S. Alofi, A. Laref, M. D. Albaqami, R. G. Alotabi and M. F. Shibl, *Nanomaterials*, 2022, **12**, 2825.
98 Y.-Y. Wu, T. Bo, J. Zhang, Z. Lu, Z. Wang, Y. Li and B.-T. Wang, *Phys. Chem. Chem. Phys.*, 2019, **21**, 19513–19520.
99 J. Rehman, T. Yu, A. El-marghany, M. F. Shibl and G. Yang, *J. Phys. Chem. C*, 2023, **127**, 23592–23600.
100 J. Hu, B. Xu, C. Ouyang, S. A. Yang and Y. Yao, *J. Phys. Chem. C*, 2014, **118**, 24274–24281.
101 S. Kaviani, A. Shamsieva, I. Piyanzina, D. A. Tayurskii and O. V. Nedopekin, *Colloids Surf., A*, 2025, **705**, 135752.

102 A. Etrini, M. Maymou, S. Oukahou, A. Elomrani, A. Benaddi, K. Sbiaai and A. Hasnaoui, *J. Phys. Chem. Solids*, 2025, 113310.
103 R. Rahimi and M. Solimannejad, *Mater. Sci. Semicond. Process.*, 2025, **192**, 109411.
104 A. Degdagui, M. Hassoun, H. Baida, K. Assiouan, A. Arhoune, M. El Hadri and F. B. Abdelouahab, *J. Energy Storage*, 2025, **140**, 118752.
105 Z. Su, S. Chen, S. Zhong, Q. Lin, D. Chen and M. Cheng, *J. Energy Storage*, 2026, **158**, 121687.
106 L. Pan, Z. Zhu and J. Duan, *Phys. Chem. Chem. Phys.*, 2026, **28**, 11088–11096.
107 H. Gao, Z. Cheng, Z.-F. Jiang and G. Chen, *Ionics*, 2026, 1–9.
108 M. E. Kassaoui, O. Zakir, K. El Maalam, O. Mounkachi and M. Ait Ali, *Phys. Chem. Chem. Phys.*, 2026, **28**, 6425–6436.
109 A. El Aiboudi, A. Sibari, Z. Mansouri, O. Mounkachi, N. Masaif and H. Ez-Zahraouy, *Phys. B*, 2025, **704**, 417041.
110 T. Bijoy, S. Sudhakaran and S.-C. Lee, *ACS Omega*, 2024, **9**, 6482–6491.
111 J. Zhang, Y.-F. Zhang, S.-P. Huang, W. Lin and W.-K. Chen, *J. Phys. Chem. C*, 2019, **123**, 30809–30818.
112 L. Shi, T. Zhao, A. Xu and J. Xu, *J. Mater. Chem. A*, 2016, **4**, 16377–16382.
113 G. Barik and S. Pal, *J. Phys. Chem. C*, 2021, **125**, 8980–8992.
114 Y.-T. Du, X. Kan, F. Yang, L.-Y. Gan and U. Schwingenschlogl, *ACS Appl. Mater. Interfaces*, 2018, **10**, 32867–32873.
115 Q. Wang, X. Wei, M. Li, Y. Zhang, Y. Yang, J. Liu, Y. Tian, Z. Li, S. Wei and L. Duan, *Phys. Chem. Chem. Phys.*, 2025, **27**, 16182–16194.
116 Q. Alam, S. Ali, A. Alanzi, M. Bououdina and L. Qiao, *Surf. Interfaces*, 2025, **62**, 106253.
117 S. R. Herabad, M. A. Mohebpour and H. R. Soleimani, *Appl. Surf. Sci.*, 2025, 165245.
118 J. Vetter, P. Novák, M. R. Wagner, C. Veit, K.-C. Möller, J. Besenhard, M. Winter, M. Wohlfahrt-Mehrens, C. Vogler and A. Hammouche, *J. Power Sources*, 2005, **147**, 269–281.
119 S. Lei, X. Chen, B. Xiao, W. Zhang and J. Liu, *ACS Appl. Mater. Interfaces*, 2019, **11**, 28830–28840.
120 D. H. Jeon, *Energy Storage Mater.*, 2019, **18**, 139–147.
121 X. Cheng, S. Li and M. Chen, *Appl. Surf. Sci.*, 2025, 163521.
122 Q. Peng, *Nanomaterials*, 2022, **12**, 3654.